engineering proceedings

MDPI

*Proceeding Paper*

# Thermal-Structural Modeling of a SiC-Based Power Module Subjected to Spatial Temperature Gradients †

**Giuseppe Mirone [1,*], Giuseppe Bua [1,2] and Raffaele Barbagallo [1]**

[1] Department of Civil Engineering and Architecture, University of Catania, Via Santa Sofia 64, 95123 Catania, Italy; giuseppe.bua@phd.unict.it (G.B.); raffaele.barbagallo@unict.it (R.B.)
[2] Department of Electrical, Electronic and Computer Engineering, University of Catania, Via Santa Sofia 64, 95123 Catania, Italy
* Correspondence: giuseppe.mirone@unict.it
† Presented at the 54th Conference of the Italian Scientific Society of Mechanical Engineering Design (AIAS 2025), Florence, Italy, 3–6 September 2025.

**Abstract**

This work presents a finite element investigation of the thermo-mechanical response of a SiC-based power module subjected to spatially non-uniform thermal gradients during active power cycling. The multilayer package, including die, solder, and encapsulant, was modeled by elastoplastic constitutive laws to capture stress and strain evolution in time and space. Two scenarios were considered: a time–space variability with fixed gradients (an initial non-uniform temperature distribution was uniformly varied in time) and a time–space variability with time-dependent gradients (an initial non-uniform temperature was non-uniformly varied in time). Results highlight critical stress concentrations at the SiC/solder interface, with plastic strains up to 5% in the solder. This study underlines the importance of transient gradient modeling for reliability assessment and fatigue life prediction of power modules.

**Keywords:** SiC-based power module; finite element thermal-structural modeling; reliability; active thermal cycling; spatial thermal gradients

## 1. Introduction

Power modules are devices that play a crucial role in the conversion of electrical energy in many engineering sectors such as automotive, aerospace, rail transportation, and renewable energies [1–3]. These systems are generally formed by a stacked sequence of metallic, ceramic and polymeric layers.

The core element of a power module is the die, a semiconductor component integrating the circuits which can be based on silicon (Si), gallium nitride (GaN) or silicon carbide (SiC) [4]. The SiC-based power modules are employed in high-power applications due to the higher operating temperature and breakdown voltage of the die. A part of the energy transmitted in the die is dissipated into heat due to the Joule effect, causing the temperature of this layer to increase (junction temperature).

Generally, multiple dies are attached to a copper–ceramic–copper substrate manufactured with techniques such as Direct Bonding Copper (DBC) and Active Metal Brazing (AMB). In these substrates, the top copper layer serves as a conductive plate for the interconnected dies, while the bottom copper layer's goal is to improve the mechanical response of the whole substrate and guarantee that the heat flow is dissipated through its interface with an external heat sink.

Check for updates

Academic Editors: Nicola Bonora, Umberto Galietti, Luigi Bruno, Davide Castagnetti, Cristiana Del Prete, Mario Guagliano and Vigilio Fontanari

Published: 25 March 2026

**Copyright:** © 2026 by the authors. Licensee MDPI, Basel, Switzerland. This article is an open access article distributed under the terms and conditions of the Creative Commons Attribution (CC BY) license.

The semi-assembled component including the dies and the copper–ceramic substrate is encapsulated with a thermosetting polymeric resin, filled with silica particles (Epoxy Molding Compound or EMC), in order to protect it against external contaminants and oxidative agents and offer insulation for the electronic circuits of the module.

Since SiC-based power modules for high-power applications can operate in harsh conditions of remarkable electric currents, the internal thermal gradients combined with the mismatching of the thermo–mechanical properties of the layers generate stresses and strains within the structure [5,6]. In particular, cyclical thermal loads represent a risk for the structural integrity of a power module [6,7], and their role in the failure of the device will be thoroughly investigated through different reliability tests [8–10].

The common reliability tests performed in the industry are divided into passive and active thermal cycles [11,12]. An active thermal cycling test consists of mounting the power module on a dedicated test bench, where a controlled pulsed electrical current is applied [13]. The current flowing through the die induces cyclic heating and cooling, governed by transients that are determined by the thermal resistance of the constituent layers.

The objective of this paper is to demonstrate that variations in temperature distribution can significantly affect the resulting stress fields and plastic strain accumulation within the package. The analysis emphasizes that the distribution profile itself may play a role comparable to, or greater than, that of peak temperatures. Accordingly, a set of idealized and purely representative stress distributions is considered to investigate the associated mechanical responses, without aiming to replicate specific thermo-mechanical loading conditions experienced during active thermal cycling of any given package.

## 2. Materials and Methods

The representative electronic package modeled for the present work is formed by a stacked sequence of the following layers: the conductive copper layer; an eutectic PbSn solder used for attaching the semiconductor die on the copper layer; the silicon carbide (SiC)-based die, which is the active element of a power module, managing the electric energy on the system; and three passivating thin-film layers of tetraethylorthosilicate (TEOS), silicon nitride ($Si_3N_4$), and polyimide used for the electrical insulation of the SiC layer and its protection against external contaminants. This assembled metallic–ceramic part is finally encapsulated with a thermosetting resin, filled with silica particles (Epoxy Molding Compound or EMC). The dimensions of the layers are reported in Table 1.

**Table 1.** Layer's geometry.

| Layer | In-Plane Dimensions [mm × mm] | Thickness [μm] |
|---|---|---|
| Copper | 8 × 12 | 1200 |
| PbSn solder | 4 × 4 | 50 |
| SiC | 4 × 4 | 200 |
| TEOS | 4 × 4 | 2 |
| $Si_3N_4$ | 4 × 4 | 1 |
| Polyimide | 4 × 4 | 6 |
| EMC | 10 × 15 | 5000 |

The modeled 3D geometry corresponds to one quarter of the full package, accounting for the double planes of symmetry of the package.

All the materials, except for copper, solder, and polyimide, were considered linear, elastic and isotropic. The plastic responses of copper, solder, and polyimide were properly accounted in the simulation, assuming the hypothesis of J2 plasticity and isotropic hardening. It is worth noting that the thermo-mechanical properties of the materials were

assumed to be equal to those at room temperature and temperature-independent, as a first approximation. The elastic constants and the elastoplastic flow curves are reported in Table 2 and Figure 1.

**Table 2.** Thermo–mechanical properties of the layers.

| Material | Young Modulus [MPa] | Poisson's Ratio [-] | Coefficient of Thermal Expansion [$10^{-6}$ 1/°C] |
|---|---|---|---|
| EMC | 25,000 | 0.34 | 12.0 |
| Copper | 125,000 | 0.3 | 17.5 |
| PbSn solder | 5600 | 0.4 | 29.0 |
| SiC | 410,000 | 0.28 | 4.0 |
| TEOS | 59,000 | 0.25 | 1.0 |
| $Si_3N_4$ | 300,000 | 0.29 | 3.4 |
| Polyimide | 3000 | 0.34 | 50.0 |

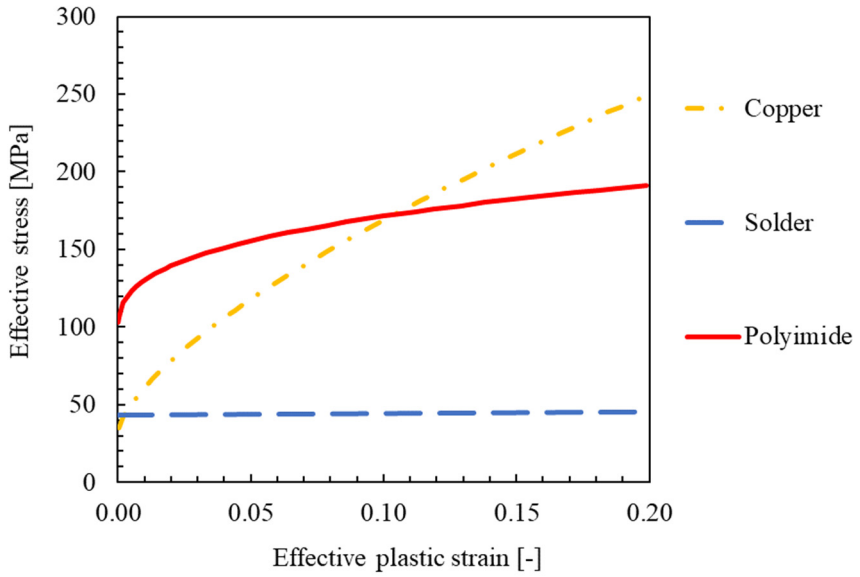



**Figure 1.** Equivalent stress vs. equivalent strain curves (flow curves): fitted data for copper (Kabaar et al. [14]), solder [15], and polyimide (Agag et al. [16]).

The novelty introduced in the present analysis lies in the different modeling of the initial conditions and boundary conditions applied to the system. In the following analysis, in order to highlight the importance of spatial temperature gradients, two representative distributions are considered with temperatures varying in both space and time so that the SiC center experiences the same thermal cycle in both cases but the overall volume of the packages undergoes rather different thermal gradients.

The first distribution is characterized by constant spatial temperature gradients (the temperature difference between the peak region and the package periphery is kept constant at 80 °C throughout the cycle), while the overall temperature level varies cyclically in time with the peak temperature oscillating between 100 °C and 160 °C.

The second distribution instead assumes a fixed instantaneous minimum temperature at the package periphery, equal to 25 °C at all times. The peak temperature follows the same temporal variation as in the first case, ranging between 100 °C and 160 °C. As a consequence, the temperature gradient and the peak-to-periphery temperature difference vary over time.

https://doi.org/10.3390/engproc2026131005

The maximum value of the temperature peak, equal to 160 °C and common to both distributions, refers to the upper temperature level imposed in passive thermal cycling to similar packages [5–7].

It is important to note that these temperature fields are not intended to reproduce any specific case of space–time temperature distribution associated with active thermal cycling. Rather, they are introduced as idealized and representative distributions, designed to isolate and highlight the effect of different temperature profiles on the resulting stress and plastic strain response of the package.

In the following sub-sections, the two temperature distributions are identified in more detail.

### *2.1. Time Independent Spatial Thermal Gradient*

Let us consider a package subjected to a single active heating–cooling thermal cycle with a total duration of $\tau$ = 100 s. The maximum temperature occurs at the hottest point of the die, located at coordinates ($x_0$, $y_0$, $z_0$), whose temporal evolution follows a triangular time–temperature profile oscillates between $T_{min}$ and $T_{max}$. An analytical expression for this thermal cycle can be conveniently represented by Equation (1).

$$T(x_0, y_0, z_0, t) = T_{min}(x_0, y_0, z_0) + \frac{2}{\pi}[T_{max}(x_0, y_0, z_0) - T_{min}(x_0, y_0, z_0)]|arcsin(sin(\omega t))|; t \in [0, \tau] \quad (1)$$

The absolute value in the equation is used to rectify the triangular waveform, which would otherwise consist of a positive and a negative half-wave of period equal to $2\tau$. With this consideration, the angular frequency $\omega$ of the thermal cycle is given by $\omega = 2\pi/2\tau = \pi/\tau = 0.0314$ rad/s. Let us consider the following scalar field, defined on a parallelepiped undeformed domain with the dimensions a x b x c as shown in Equation (2), where T($x_0$, $y_0$, $z_0$, t) is the function reported in Equation (1); $\rho$ is the distance between the generic point P(x, y, z), belonging to the spatial domain, and the hottest point of the package ($x_0$, $y_0$, $z_0$); and k is the real parameter which regulates the temperature gradient along the radial coordinate $\rho$.

$$T(x, y, z, t) = T(x_0, y_0, z_0, t) - k\,\rho^2(x, y, z) \quad (2)$$

It can be observed from Equation (2) that all points located at the same distance from the hottest point of the die share an identical temperature, implying a spherical temperature distribution. If the parameter *k* is assumed to be time-independent, the spatial temperature gradient consequently remains constant over time.

To determine the value of *k*, a specific temperature gradient must be imposed at a given time instant. Physically, at $t$ = 0 s, all points within the package are expected to have a uniform temperature of $T$ = 25 °C, which would lead to $k$ = 0. Therefore, the evaluation is performed at $t = \tau/2$ = 50 s, corresponding to the maximum temperature. At this time, the imposed condition is that the temperature difference $\Delta T$ between the hottest point, located at ($x_0$, $y_0$, $z_0$) = (0, 1.35, 0) mm, and the farthest point in the package, (a, b, c) = (5, 5, 7.5) mm, equals 60 °C. The corresponding distance between these two points is $\rho^*$ = 9.725 mm, from which the *k* factor can be calculated as follows:

$$k = -\frac{\left(T_{(a,b,c)} - T_{(x_0,y_0,z_0)}\right)}{\rho^{*2}} = 0.634\ \frac{°C}{mm^2} \quad (3)$$

Once the value of k is fixed (or a time-independent spatial $\Delta T$ is imposed), it becomes evident that if the initial temperature of the SiC is assumed to be 25 °C, at t = 0 s, then, at the furthest point from the SiC hotspot, the temperature predicted by the present model

would be −35 °C. This clearly indicates that, to accurately capture the evolution of spatial temperature gradients over time within the package, the parameter k should be defined as a time-dependent function. However, to preserve the simplicity of a constant-gradient model, it is assumed here that at t = 0 s the temperature at point (a, b, c) equals 25 °C, corresponding to 85 °C at the SiC hotspot, while at t = 50 s the maximum temperature rises to 160 °C, with 100 °C at the point farthest from the hotspot.

Figure 2a reports the package model with possible paths, along which the temperature trends at different times can be observed for getting the picture of its variability in time and space. Considering Case 1, Figure 2b reports the time variability of the temperature at three reference points, i.e., the SiC center, the SiC/Resin interface center and furthest point of the model from SiC center. Figure 2c,d show the space variability temperature distributions along path#2, extending from the center of the model to its outer lateral surface, at the beginning and at the top temperature point of a cycle.

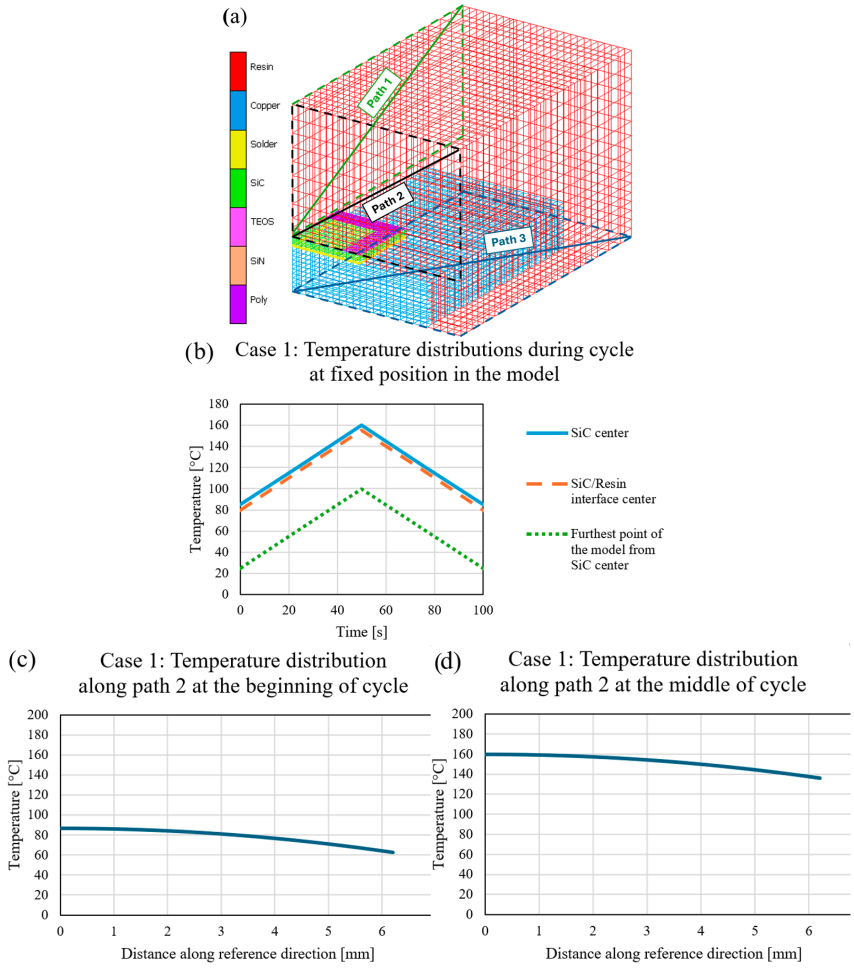



**Figure 2.** Identification of the paths along which temperature is evaluated (**a**). Case 1: Temperature histories at fixed positions of the model (**b**) and temperature spatial distribution along path 2 at the beginning of the cycle (**c**) and at the middle of the cycle (**d**).

To summarize, in Case 1 the temperature varies in time and in space, but the shape of the space variability (gradient) is constant in time.

### *2.2. Time Dependent Spatial Thermal Gradient*

Let us now consider the temperature field defined by Equation (2). The physical phenomenon to be simulated is a temperature difference ($\Delta T$) between the SiC hotspot

and the point located at the maximum distance from it, which starts from zero at t = 0 s, increases linearly over time up to 60 °C, at t = $\tau/2$, and then returns to zero.

For this purpose, the triangular waveform previously introduced in Equation (1) can be recalled and employed as shown in Equation (4).

$$k(t) = k_{max}\frac{2}{\pi}|\arcsin(\sin(\omega t))| = -\frac{T(x,y,z,t) - T(x_0,y_0,z_0,t)}{\rho(x,y,z)^2} \quad (4)$$

Considering that the function $T(x_0, y_0, z_0, t)$ is the one given in Equation (1), the temperature field with a linearly time-varying gradient is expressed by Equation (5).

$$T(x,y,z,t) = T_{min}(x_0,y_0,z_0) + \frac{2}{\pi}|arcsin(sin(\omega t))|[T_{max}(x_0,y_0,z_0) - T_{min}(x_0,y_0,z_0) - k_{max}\,\rho^2(x,y,z)] \quad (5)$$

Case 1 refers to conditions where the lower temperatures of the cycle are around 80 °C below the higher ones at each location of the package (uniform temperature variations in time), while the temperature gradient is such that the package center is always 60 °C hotter than the package lateral surface during the cycle.

Instead, Case 2 refers to conditions where the package is at uniform room temperature at the cooler stage of the cycle and gets to a higher non-uniform spatial distribution of the hotter stage of the cycle (non-uniform temperature variations in time), where the peak temperature at the hotter stage of the test is the same as in Case 1.

Considering Case 2, Figure 3a reports the time variability of the temperature at three reference points, i.e., the SiC center, the SiC/Resin interface center and furthest point of the model from SiC center. Figure 3b,c show the space variability temperature distributions along path#2, extending from the center of the model to its outer lateral surface, at the beginning and at the top temperature point of a cycle.

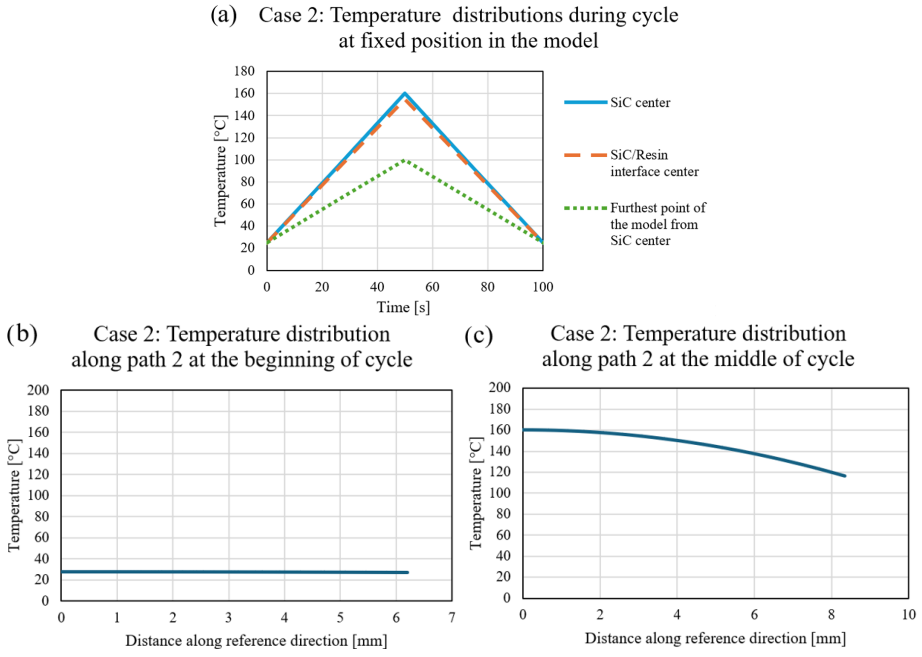



**Figure 3.** Case 2: Temperature histories at fixed positions of the model (**a**) and temperature spatial distribution along path 2 at the beginning of the cycle (**b**) and at the middle of the cycle (**c**).

The two thermo-mechanical load histories proposed here can be taken as representative of operating conditions for a package; in fact, for a given temperature distribution at the hotter stage of a cycle (e.g., a gradient from 160 °C at the package center to around 100 °C at the package outer side surface), realistic temperature distributions at lower temperature

stages of a cycle can be included between the two extremes of uniformly lower temperatures (uniform cooling, e.g., 60 °C below everywhere) and a uniform 25 °C temperature (complete cooling down to room temperature).

## 3. Results and Discussion

The stresses distributions were analyzed at two specific time instants during the thermal cycle applied to the package: at the peak temperature (t = 50 s, corresponding to the mid-cycle) and at the end of the cooling phase (t = 100 s). At these two instants, the components of the stress tensor were plotted along six interfaces of the package (it should be noted that the origin of each path lies on the package's axis of symmetry, i.e., the *y*-axis):

- Interface 1: copper/solder in the first segment of the path; copper/resin in the second segment.
- Interface 2: solder/SiC.
- Interface 3: SiC/resin in the initial segment; SiC/TEOS in the final segment where the contact with the passivating frame begins.
- Interface 4: TEOS/$Si_3N_4$ (and a short section of TEOS/polyimide near the edge of the double passivation).
- Interface 5: $Si_3N_4$/polyimide.
- Interface 6: polyimide/resin.

All the analyzed paths and their corresponding interfaces are shown in Figure 4. The distributions of the stress components are arranged into three columns. The first column presents the components that remain continuous across the interfaces, namely the interfacial normal stress and the two interlaminar shear stresses. The second and third columns display the components that exhibit discontinuities when transitioning from material A to material B, specifically the two in-plane normal stresses and the in-plane shear stress, respectively.

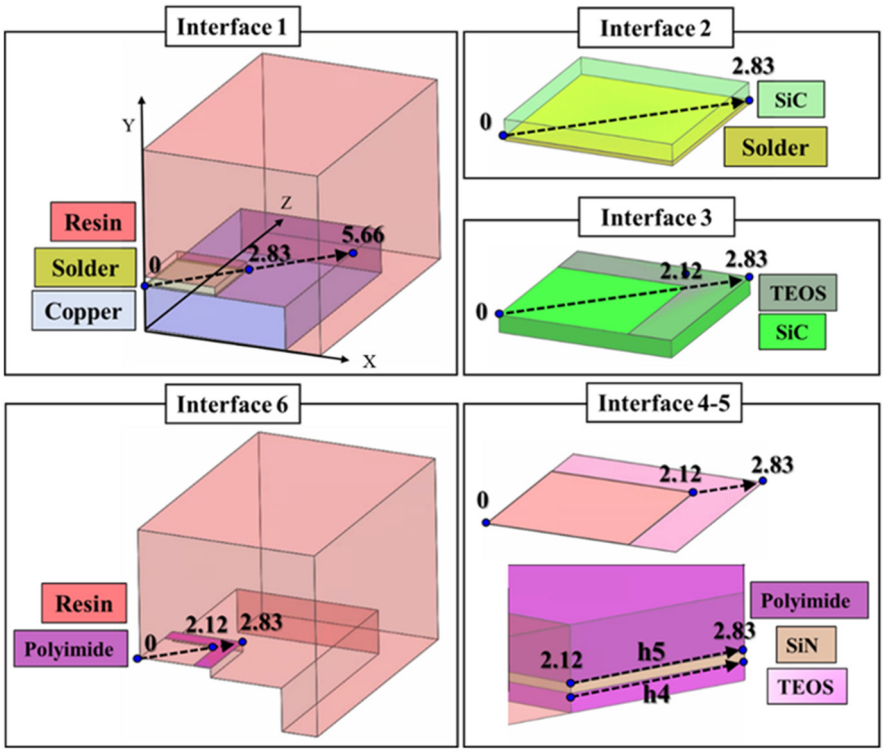



**Figure 4.** Paths and interfaces where stress components were extracted.

### *3.1. Case 1: Time-Indepenent Spatial Thermal Gradient*

#### 3.1.1. C1: Stress Distributions at Mid-Cycle (t = 50 s, Maximum Temperature)

As shown in Figure 5, where the stress subscripts 1, 2, and 3 correspond to the x, *y*, and z directions depicted in Figure 4, at interface 1 (copper/solder and copper/resin), the interfacial stress components exhibit pronounced local variations near the material transitions. In particular, the interfacial normal stress σ22 decreases from a plateau value of approximately 10 MPa at the copper/solder interface to nearly zero at the copper/resin interface. Simultaneously, the interlaminar shear components display similar magnitudes (in absolute value) and a monotonic increase from zero to 20 MPa, followed by a rapid decrease to zero within the transition region. Outside this region, on both the copper and solder (or resin) sides, the in-plane shear stress remains negligible. The copper layer is predominantly subjected to compressive stresses ($\sigma 11 = \sigma 33 \approx -20$ MPa), as is the solder ($\sigma 11 = \sigma 33 \approx -10$ MPa), whereas the resin region experiences a tensile stress state ($\sigma 11 = \sigma 33 \approx 10$ MPa).

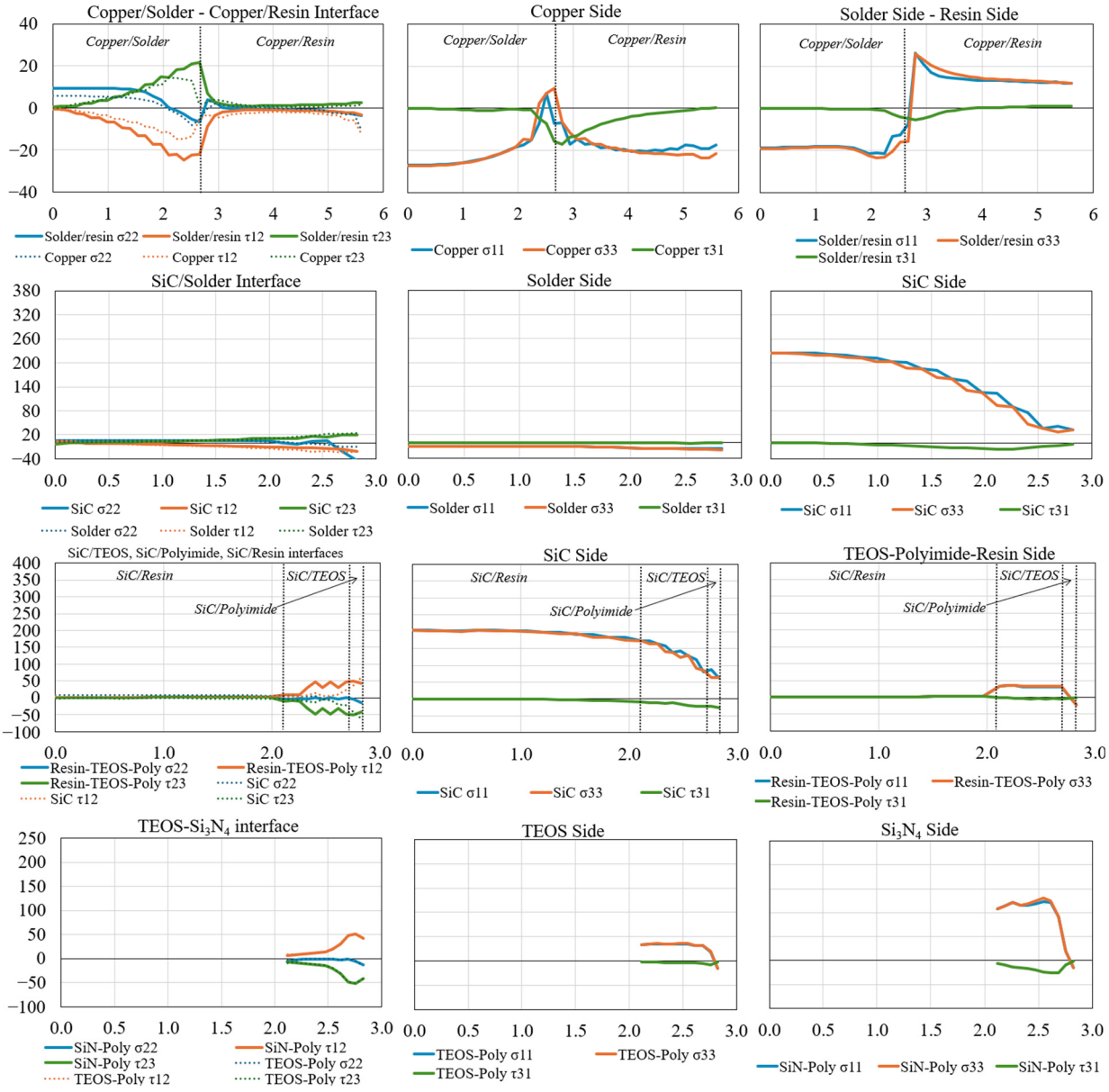



**Figure 5.** *Cont.*

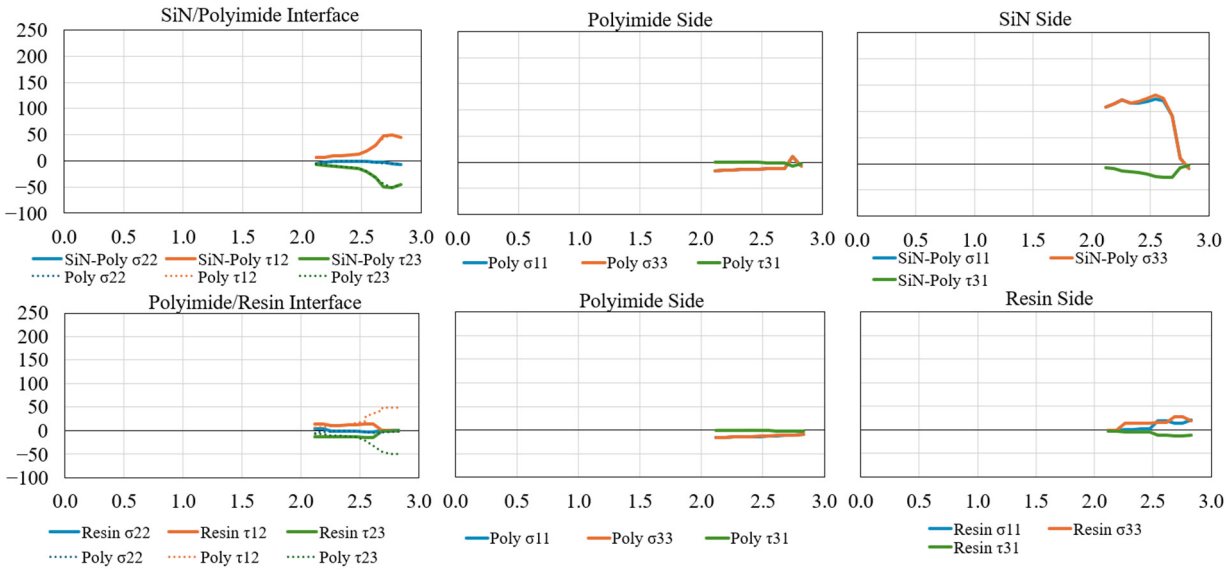



**Figure 5.** First case of spatial thermal gradient: stress components (y axes [MPa]) plotted along the interfaces considered in Figure 4, at t = 50 s (mid-cycle) (x axes [mm]).

At interface 2 (solder/SiC), the SiC layer exhibits significantly higher stress levels: both σ11 and σ33 reach a maximum of about 210 MPa at the layer center, progressively decreasing to approximately 30 MPa near the die edges.

In the passivation frame, the in-plane normal stresses reach approximately 40 MPa in the TEOS region and 120 MPa in the $Si_3N_4$ region, confirming the presence of a steep stress gradient through the thickness of the passivation stack.

#### 3.1.2. C1: Stress Distributions at the End of Thermal Cycle (t = 100 s)

As shown in Figure 6, at the end of the thermal cycle applied to the package, almost all six considered interfaces are unstressed. This can be explained by the fact that the ductile layers accumulate negligible plastic strains along the thermal history modeled in this specific case. In fact, as already discussed in the work of Mirone et al. [6], if all layers were modeled as purely elastic materials, then the entire package, at the end of the cooling phase, would return to its initial mechanical state (undeformed and stress-free). For elasto-plastic layers, when the accumulated plastic strains are relatively small, the residual stresses after a single thermal cycle can be considered negligible. The only interface exhibiting appreciable internal stresses is the copper/solder interface. On the copper side, the in-plane normal stress components reach a maximum of approximately 30 MPa at the center of the package and progressively decrease toward the copper/resin interface, where they completely vanish. This behavior is consistent with the distribution of accumulated plastic strains observed in the subsequent layers—copper, solder, and polyimide—which confirms the localization of plastic deformation primarily near the copper/solder transition.

#### 3.1.3. C1: Distribution of Plastic Strains in Ductile Layers at Mid-Cycle and at the End of Cooling Phase

As illustrated in Figure 7, the residual plastic strains accumulated at the end of the thermal cycle in interfaces involving elasto-plastic materials remain below 1.5%. The highest plastic strain occurs in the solder layer at the interface with the SiC, near the sharp corner edge, where a local stress concentration is expected.

https://doi.org/10.3390/engproc2026131005

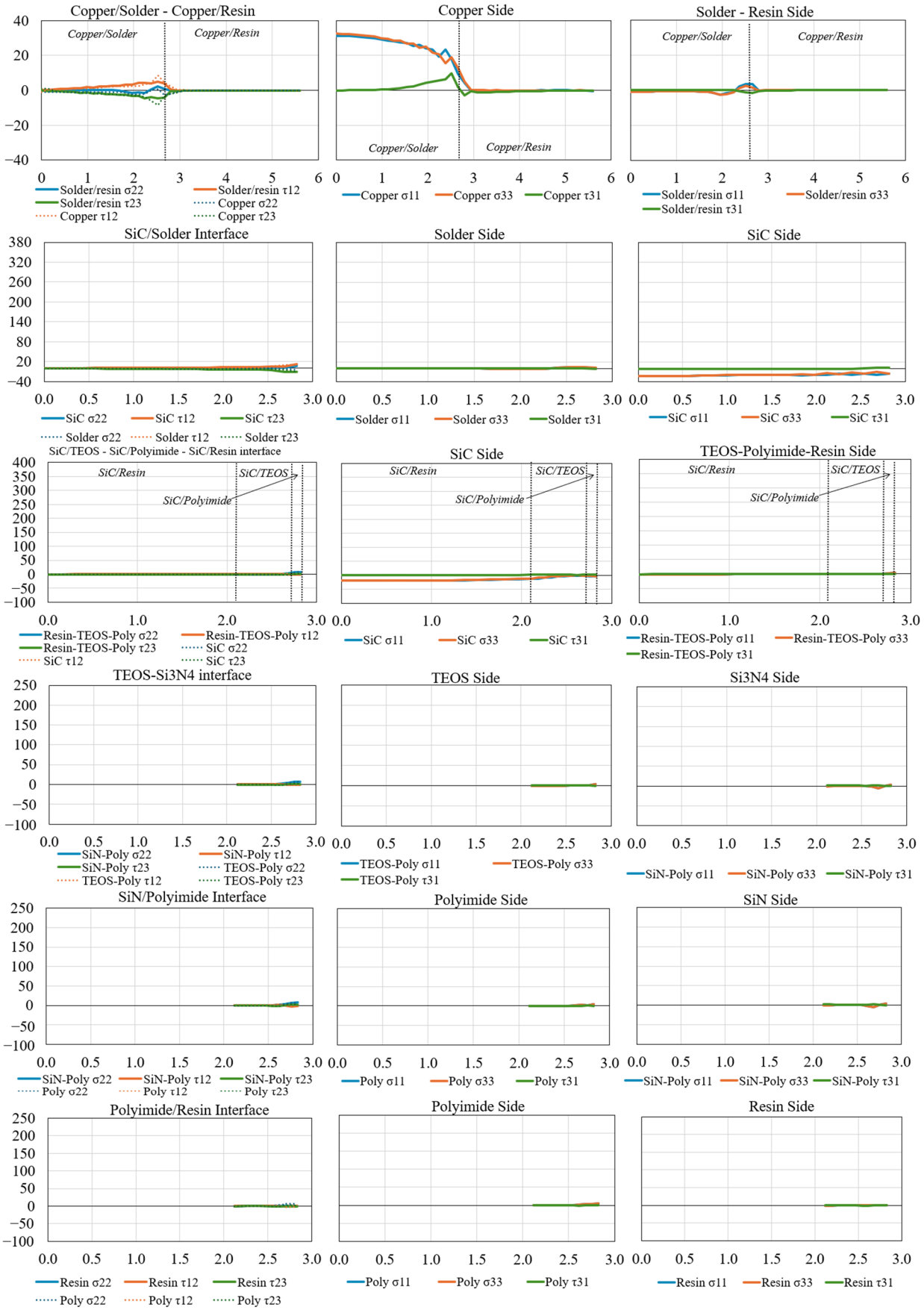



**Figure 6.** First case of spatial thermal gradient: stress components (y axes [MPa]) plotted along the interfaces considered in Figure 4, at t = 100 s (end of cooling phase) (x axes [mm]).

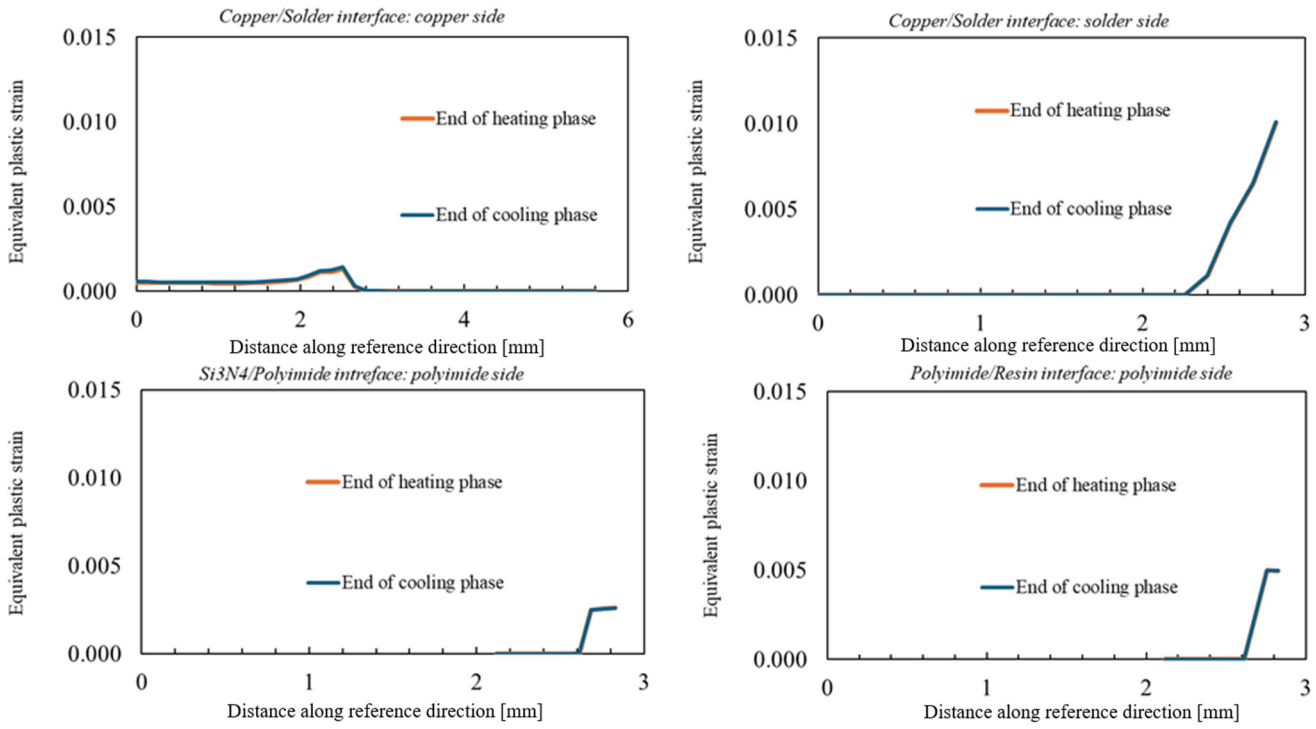



**Figure 7.** First case of spatial thermal gradient: distributions of equivalent plastic stains, along four elastoplastic interfaces, at mid-cycle ($t$ = 50 s) and at the end of cooling phase.

At the copper/solder interfaces, the plastic strain distribution on the copper side is nearly uniform in the central region of the package (≈0.05%) and increases toward the transition zone with the resin, reaching approximately 0.15%.

For the interfaces involving polyimide, located at the edges of the passivation layers (TEOS and $Si_3N_4$), the maximum plastic strains appear at the outer sharp edge of the frame, with values on the order of a few per ten thousand. Slightly higher values, up to about 0.5%, are observed in the polyimide frame at the interface with the resin.

It should be noted that these results may be influenced by the local mesh refinement in the vicinity of the sharp corners, which can affect the accuracy of strain estimation in regions of steep stress gradients.

### *3.2. Case 2: Time Dependent Spatial Thermal Gradient*

#### 3.2.1. C2: Stress Distributions at Mid-Cycle ($t$ = 50 s, Maximum Temperature)

In the second case, characterized by a time-dependent spatial temperature gradient model, it is clearly observed that the hottest point of the package (within the die) undergoes a greater thermal excursion compared to the case with a temporally constant temperature gradient. Specifically, at this location, the temperature variation ($\Delta T$) at peak heating in Case 1 was 75 °C, whereas in Case 2 the same point experiences a $\Delta T$ of 135 °C at mid-cycle. It is therefore expected that the layers surrounding the die in Case 2 are subjected to higher mechanical stresses than in Case 1.

As shown in Figure 8, at the copper/solder interface, the normal stress component perpendicular to the interface is approximately uniform and positive (tensile), with a magnitude of about 10 MPa. This value progressively decreases, eventually changing sign, towards the transition zone near the copper/resin interface, where it becomes nearly zero.

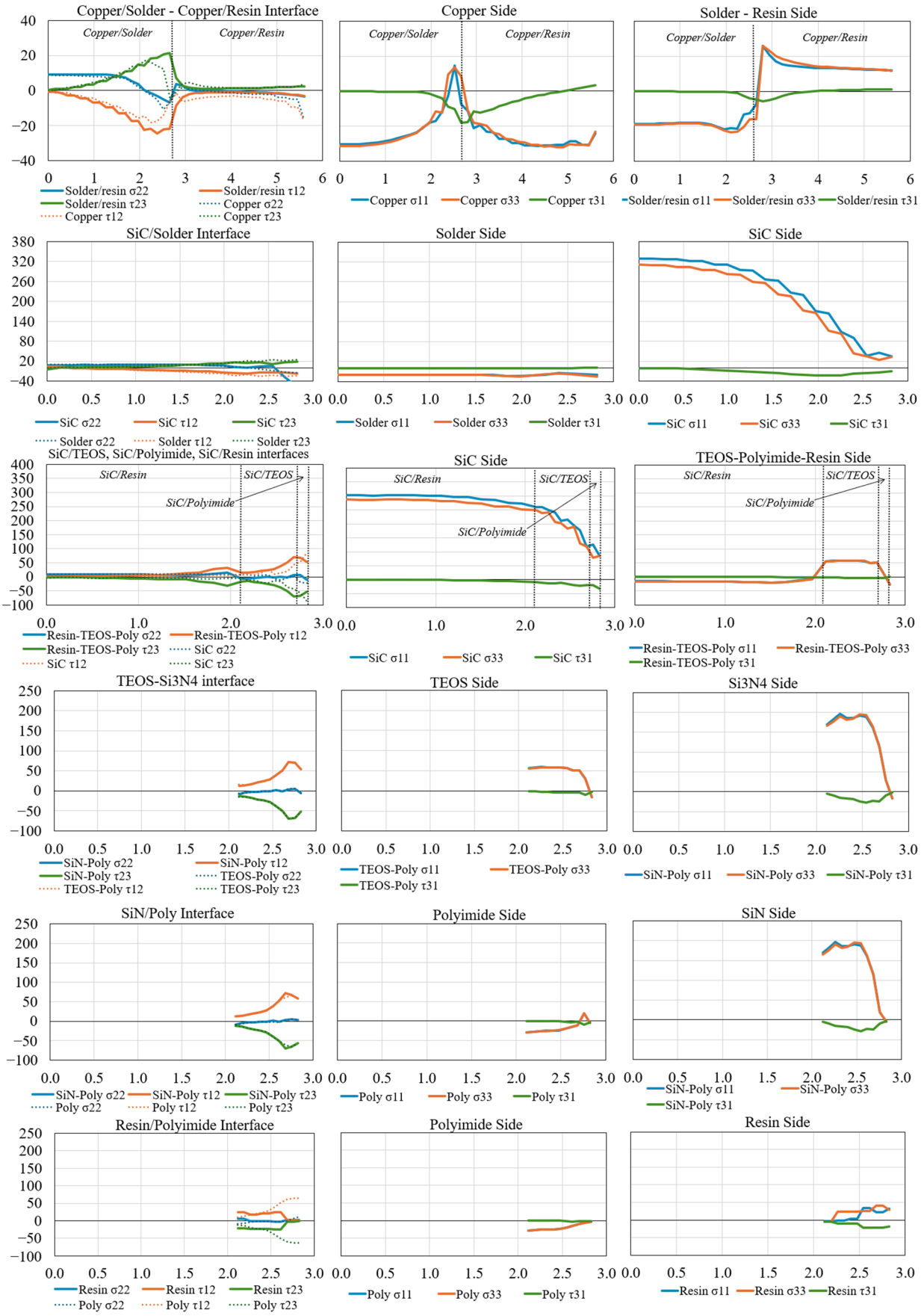



**Figure 8.** Second case of spatial thermal gradient: stress components (y axes [MPa]) plotted along the interfaces considered in Figure 4, at t = 50 s (mid-cycle) (x axes [mm]).

https://doi.org/10.3390/engproc2026131005

The interlaminar shear stresses along the copper/solder interface increase in absolute value from zero at the center of the package, reaching a peak of approximately 20 MPa in the transition region close to the copper/resin interface. Along the latter interface, these shear stresses tend to vanish.

The in-plane normal stresses within the copper layer exhibit a parabolic distribution, ranging from −30 MPa (compressive) at the center of the package, to about 15 MPa near the copper/resin transition, returning to −30 MPa in the copper region directly bonded to the resin. On the opposite side of the interface, the in-plane normal stresses in the solder layer are approximately −20 MPa (compressive), transitioning to an average value of 15 MPa within the resin layer. The in-plane shear stresses remain negligible throughout.

As in the previous configuration, at the SiC/solder interface, the most critical stresses—specifically the in-plane normal components within the SiC layer—exhibit pronounced gradients. At the center of the SiC, the in-plane normal stress reaches a peak value of about 300 MPa, progressively decreasing to approximately 30 MPa near the outer edge of the layer. This represents an increase relative to the previous case, where the peak value was approximately 220 MPa.

Within the passivation frame, the in-plane normal stresses attain plateau values of roughly 50 MPa in the TEOS layer, which is about 10 MPa higher than in the previous configuration, and approximately 180 MPa in the $Si_3N_4$ layer, corresponding to an increase of 55 MPa compared to Case 1.

#### 3.2.2. C2: Stress Distributions at the End of Thermal Cycle (t = 100 s)

As observed from the diagrams in Figure 9, also in this second case, some material interfaces return to being stress-free at the end of the thermal cycle, while those involving elastoplastic materials, having accumulated plastic strains, exhibit residual stresses. At the copper/solder interface, residual interlaminar shear stresses of approximately 20 MPa are observed in the transition zone toward the copper/resin interface. On the copper side, at the end of the heating phase, the residual in-plane normal stresses are relatively uniform toward the center of the package, reaching values of approximately 40 MPa in tension and progressively decreasing toward the resin-adjacent regions.

At the SiC/solder interface (SiC side), the in-plane normal stresses are compressive and range from −85 MPa at the center of the package to −20 MPa at the outer edge of the SiC. If Case 1 had been considered, these latter stresses—at the end of the thermal cycle—would have been nearly negligible (Figure 9). This clearly demonstrates that the modeling approach adopted for the time-dependent spatial–thermal gradients has a significant influence on the resulting stress distributions.

Finally, at the $Si_3N_4$/polyimide interface, both the residual interfacial stresses and the in-plane normal and shear stresses are more concentrated in the transition zone between the two passivation frames. The $Si_3N_4$ frame is laterally surrounded by polyimide, a material that could exhibit high plastic strain. As a result, plastic deformation is localized in this region. At the polyimide/$Si_3N_4$ interface, interfacial stresses peak at the outer edge of the polyimide frame, all reaching approximately 25 MPa in absolute value. In-plane normal stresses on the silicon nitride side reach a negative peak value of −35 MPa (compression) in the transition zone toward the polyimide frame, while the in-plane shear stress component reaches a maximum of about 25 MPa at the same location.

https://doi.org/10.3390/engproc2026131005

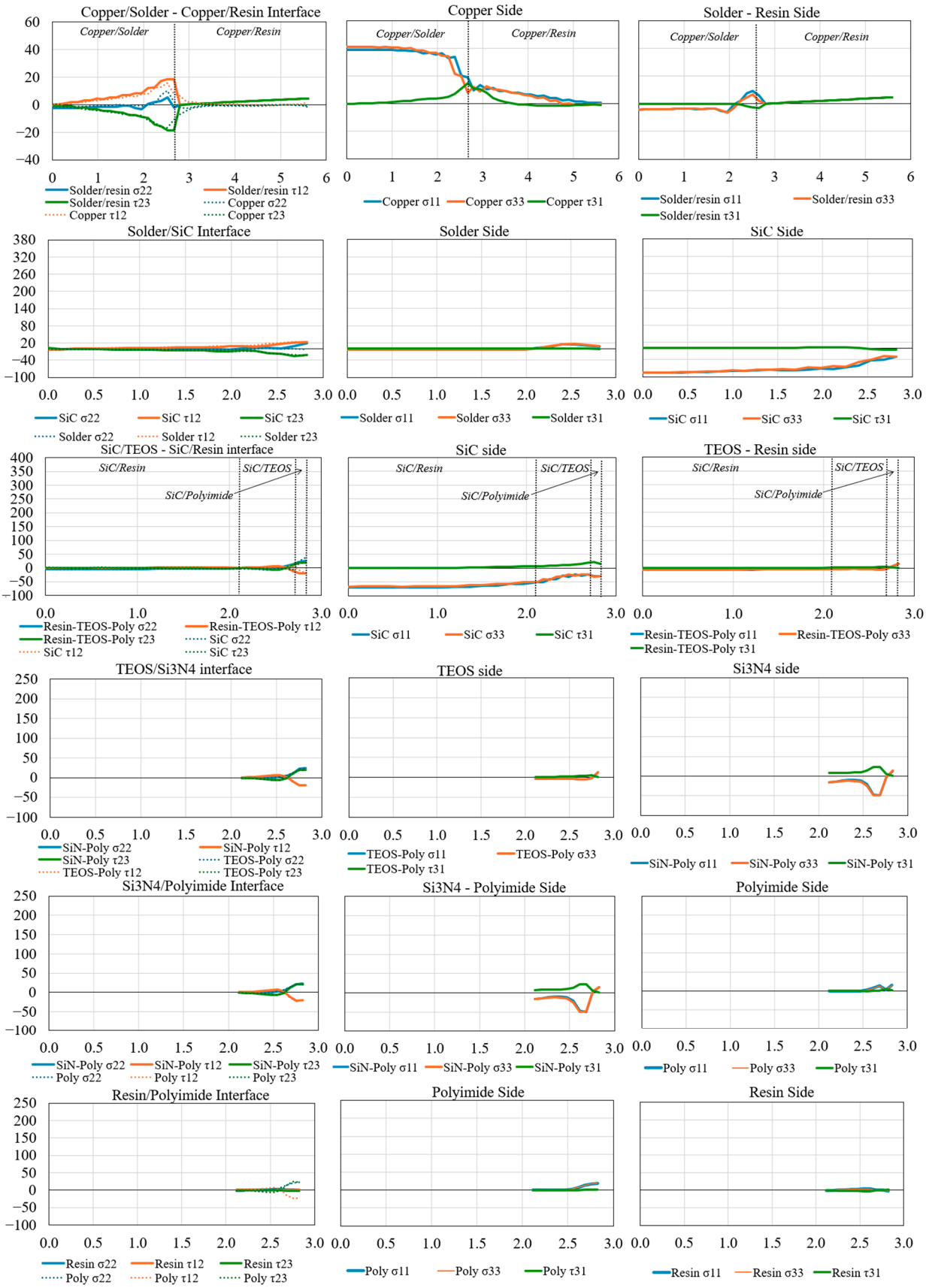



**Figure 9.** Second case of spatial thermal gradient: stress components (y axes [MPa]) plotted along the interfaces considered in Figure 4, at t = 100 s (end of cooling phase) (x axes [mm]).

https://doi.org/10.3390/engproc2026131005

#### 3.2.3. C2: Distribution of Plastic Strains in Ductile Layers at Mid-Cycle and at the End of Cooling Phase

As shown in Figure 10, the trends of the plastic strain distributions, both at the end of the heating phase and at the end of the thermal cycle, are similar to those observed in Case 1 but with higher peak values, as expected. At the copper/solder interface, the copper continues to accumulate plastic strain even after reaching the maximum temperature. The plastic deformation is uniformly distributed across the central regions of the package, with an average value of approximately 2.3% along the initial segment of the path at the end of the thermal cycle. The peak plastic strain at the end of the cycle reaches approximately 3.8 ‰ in the transition zone near the copper/resin interface.

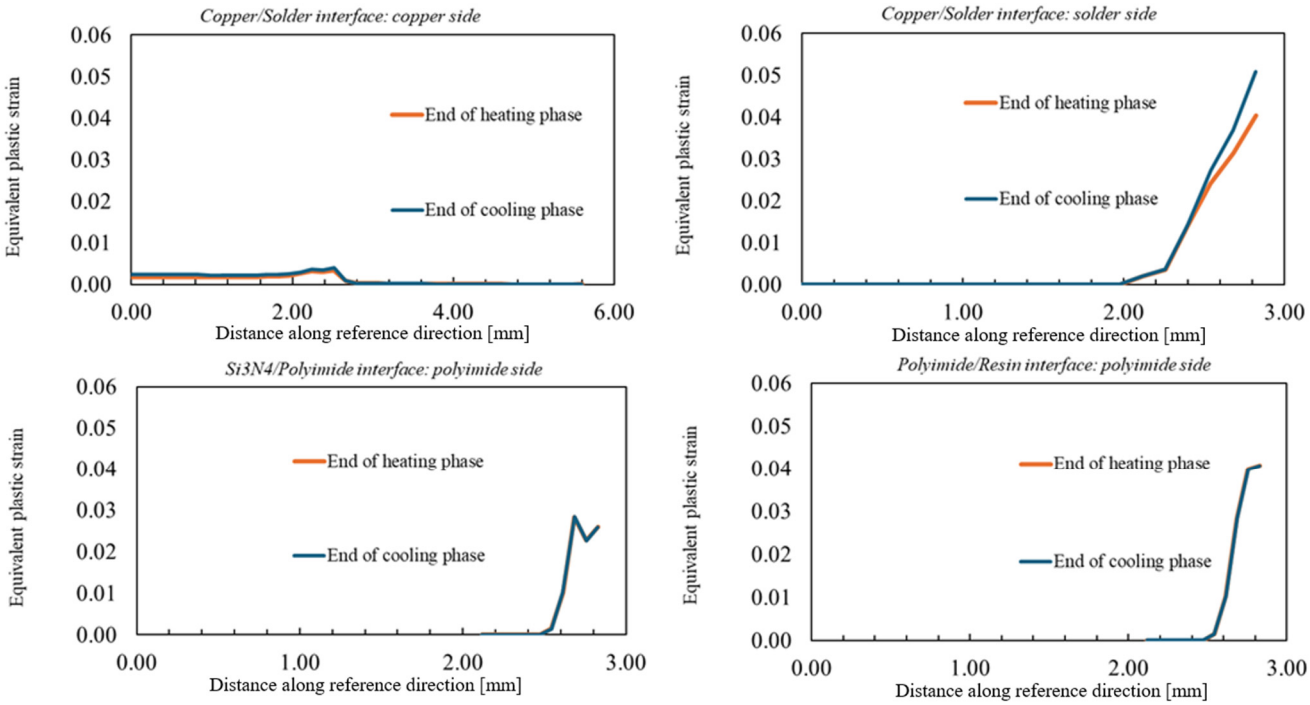



**Figure 10.** Second case of spatial thermal gradient: distributions of equivalent plastic stains, along four elastoplastic interfaces, at mid-cycle (t = 50 s) and at the end of the cooling phase.

The solder undergoes an additional 1% of plastic strain during the cooling phase, increasing from a maximum of 4% up to 5% at the most stressed location, namely the sharp corner edge.

Polyimide is the only layer that does not exhibit any further accumulation of plastic strain during the second part of the cycle. The maximum plastic strain in this layer is localized at the interface with the encapsulant resin, close to the outer edge. In this region, the plastic strain at the end of the thermal cycle is approximately 4%.

### *3.3. Comparison of the Mechanical Response at Significant Locations of the Model*

In order to highlight the effects of thermal gradients in determining the thermo-mechanical response of a package, stresses and plastic strains are compared for both simulated cases at meaningful points within the package.

The centroid of the SiC volume undergoes the same cycling of temperature in both Case 1 and Case 2, ranging between 100 and 160 °C. Therefore, the corresponding points at the two closest interfaces, SiC-Solder and SiC-Resin, are perfect to isolate the effect of temperature gradients from that of the absolute values of temperature in inducing thermomechanical stresses in the package.

https://doi.org/10.3390/engproc2026131005

Similar considerations apply for the location selected to compare plastic strains, whereas the most critical plastic strains in the package are identified at the interfaces of solder–SiC and solder–copper, closer to the outline of the SiC rather than at its center, which is quite obvious considering that the high elastic stiffness of SiC limits large strains also in closely neighboring materials.

Figure 11 illustrates the points where the stresses induced by both temperature distributions are compared to each other.

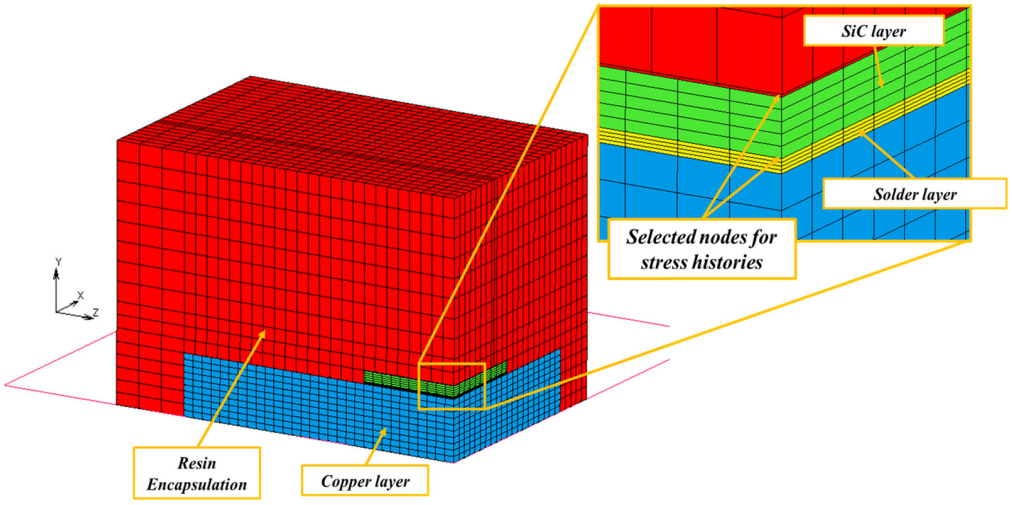



**Figure 11.** Locations of stress comparisons.

Mid-Cycle (end of the heating phase): The in-plane normal stresses at the center of the top and bottom surfaces of the SiC–solder interface at mid-cycle are magnified nearly 50% by the temperature gradients of Case 2, being larger than those of Case 1, despite the same local temperature cycling between 100 °C and 160 °C. In fact, the plots in the left column of Figure 12 show changes in tensile stresses from around 200 to 300 MPa. Greater magnifications of the same stresses (factor close to 3) take place in softer materials, seen in the right column of Figure 12, as the resin undergoes compressive stresses, changing from 5 MPa to 15 MPa, and the solder changes from 7 MPa to 20 MPa. The in-plane shear stress is negligible in both cases.

End-cycle (end of cooling phase): Different residual stresses are visible at the end of the plots in Figure 12, highlighting that different plastic strains are inducing different permanent deflections of the package.

Now, the stresses are smaller than they were after heating, but the relative differences induced by the two imposed temperature gradients are greater than before: end-cycle stresses from Case 1 to Case 2 change from roughly 30 to 90 MPa at both surfaces of the SiC and from roughly 2 to 6 MPa at the lower surface of the resin and upper surface of the solder.

Stress reversal on SiC: It is also worth noting that the stress at the SiC surfaces is compressive after heating; at end cycle it becomes tensile. Instead, on the resin and the solder the stress is tensile over the whole temperature cycle. This is consistent with the role of the SiC, which is very small, thin and rigid, acting as a hard inclusion embedded in a softer matrix that is partially elastic (the resin) and partially elastoplastic (the solder).

Looking at Figure 13, lower differences are observed for the out-of-plane normal stresses (direction 2,2), which at mid-cycle is tensile and changes from 5 MPa in Case 1 to 8 MPa in Case 2. This stress is almost uniform across all points of both interfaces (upper solder, lower SiC, upper SiC, lower resin), as the through-the-thickness normal stress cannot change significantly along the 0.2 mm thickness of the SiC.

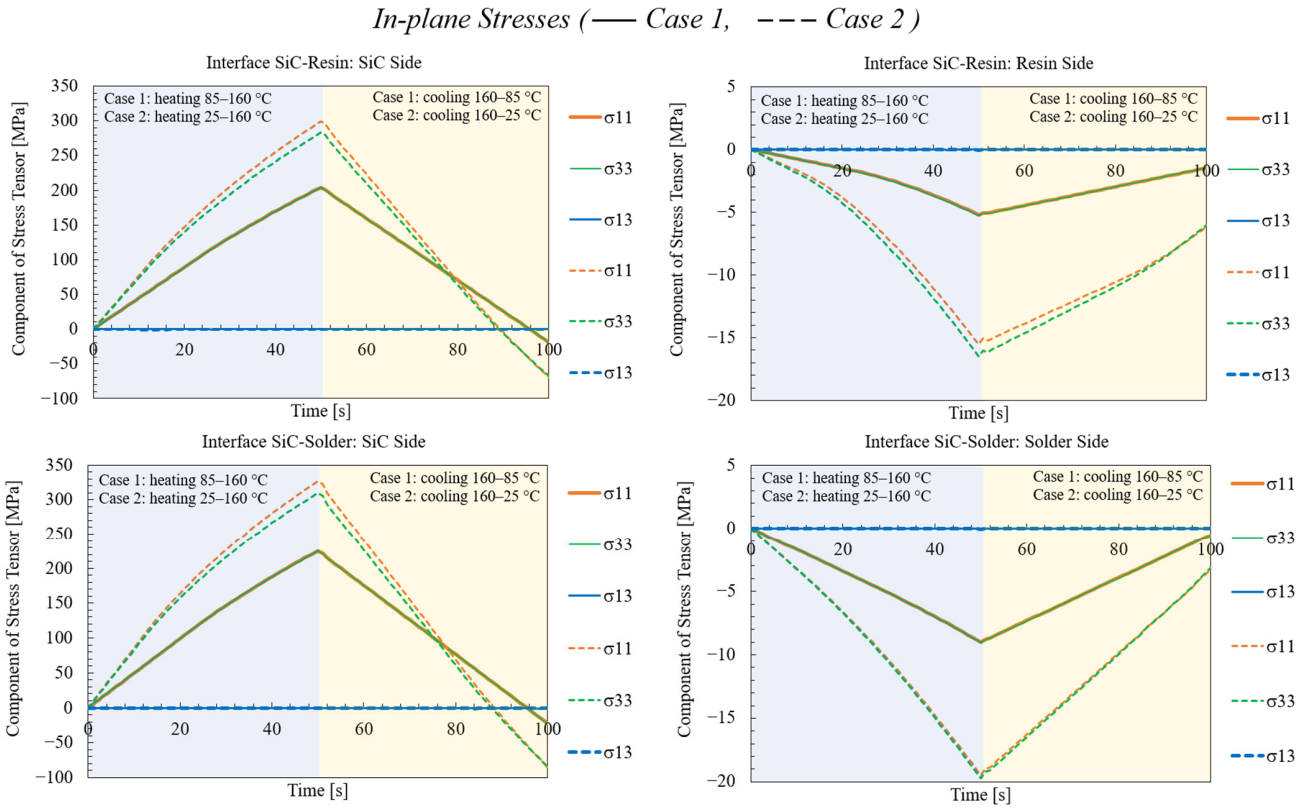



**Figure 12.** In-plane stresses at selected locations in the package.

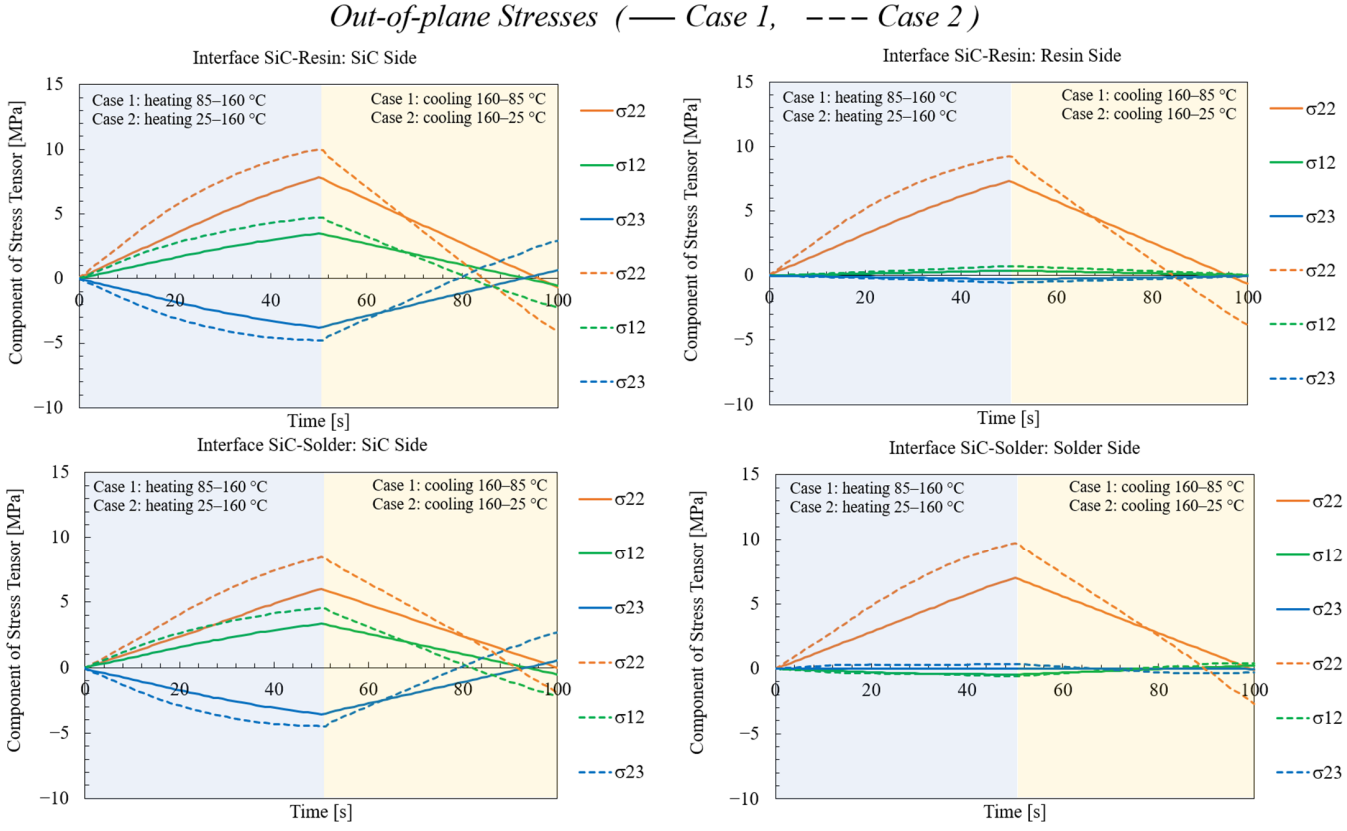



**Figure 13.** Out-of-plane stresses at selected locations in the package.

https://doi.org/10.3390/engproc2026131005

At end-cycle, such out-of-plane normal stresses are reversed to a compressive sign; in particular, stress induced by the temperature distribution of Case 1 is below 1 MPa, while stress from Case 2 is around 3 MPa.

The out-of-plane shear stresses vary around almost negligible values well below 1 MPa.

Although the temperature distributions adopted in this study are representative, an overall connection with common parameters typical of power electronics testing was provided by selecting the upper peak temperatures of both cases equal to the maximum temperature that was actually adopted in passive thermal cycling for similar packages [4–7].

Similarly, the order of magnitude of the stresses predicted above can be compared to failure stresses from the literature [7] for the various materials involved in the analyses, as summarized in Table 3.Then, even if no structural integrity or damage-related considerations are done in this work, it is confirmed that the predicted stresses are fully compatible with the corresponding limit stresses, as the simulated thermo-mechanical loads are referrable to those of usual passive thermal cycling procedures.

**Table 3.** Admissible stresses of the materials from the literature.

| | Solder | SiC | Copper | Polyimide | Resin | SiN |
|---|---|---|---|---|---|---|
| Admissible stress [MPa] | 52–80 | 180–270 | 155–330 | 65–80 | 14–300 | 500–700 |
| References | [15,17] | [18] | [14] | [19] | [20,21] | [22] |

Finally, the plastic strain evolution generated by the two time- and space-dependent temperature distributions was evaluated at the critical location depicted in Figure 14.

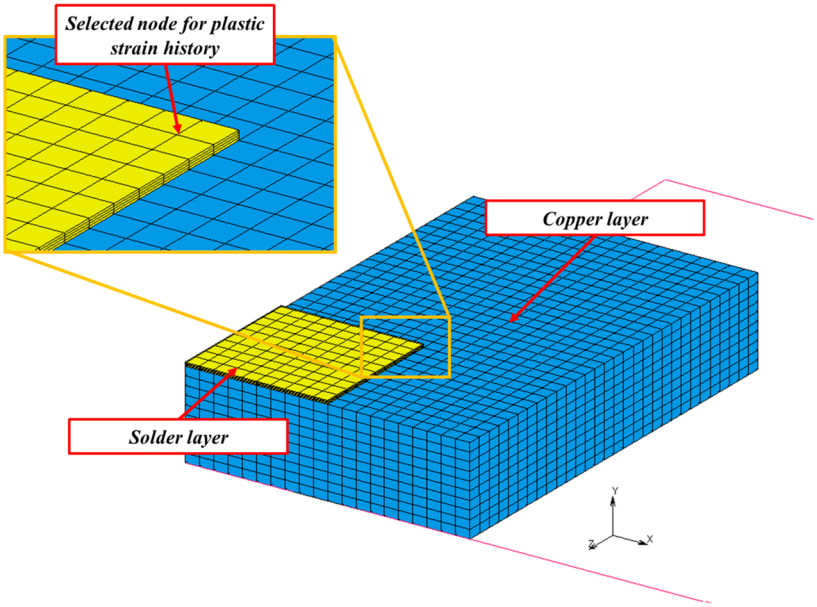



**Figure 14.** Location of plastic strains acquisitions.

Figure 15 shows that, again, the two different temperature distributions induce remarkably different histories of plastic strain of the solder locations close to the SiC center, despite the local temperature there evolving identically between 100 and 160 °C in both cases.

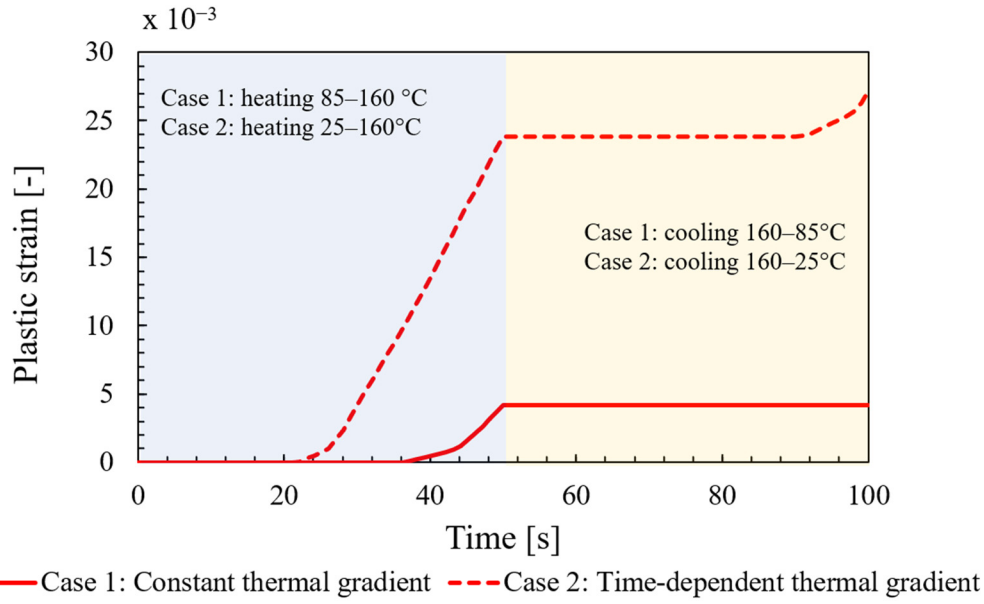



**Figure 15.** Histories of plastic strain at selected locations in the package.

The solder under the SiC edges starts yielding at rather different temperatures depending on the temperature gradient, i.e., only slightly above room temperature for the steeper gradients of Case 2 and around 35 °C for the blunter gradients of Case 1. At mid-cycle, very different plastic strains are accumulated in the solder, as the sharper temperature gradients of Case 1 induce a 2.5% plastic strain, five times greater than the 0.5% plastic strain promoted by the flatter temperature gradient of Case 1.

In both cases, an elastic unloading phase starts as the package begins cooling down and the permanent plastic strain remains constant. The Case 1 temperature gradients do not trigger any further plastic straining until end-cycle; instead, the Case 2 temperatures induce a further small increment of plastic strain at the final cooling stages.

These considerations prove that the effect of spatial temperature distributions far from the SiC is crucial in determining plastic straining in the solder close to the SiC edges and also assessing the order of magnitude of such an effect for the representative temperature gradients considered here.

## 4. Conclusions

In this work, the thermo-mechanical response of a SiC-based power module subjected to spatial thermal gradients was investigated, simulating the typical condition of an active power cycle. Unlike passive thermal cycling, the active one induces faster temperature transients and remarkable temperature variation, particularly within the semiconductive die, where power is dissipated due to the Joule effect.

In order to model the thermal field derived from the self-heating of the device, two different spatial temperature field scenarios were analyzed: one assuming a time-invariant spatial gradient, and the other introducing a time-dependent temperature distribution. A spherical distribution was assumed in both cases, fixing the highest temperature in correspondence of the center of SiC layer. In the first case, a temperature difference between the hotspot and the external boundary was imposed throughout the cycle, while in the second, the thermal gradient evolved with the time, reaching its peak at mid-cycle and returning to zero at the end.

The mechanical response of the package was evaluated extracting the stresses and plastic strain distributions at interfaces involving elasto-plastic layers. Results revealed that

during the heating phase (mid-cycle), substantial thermal stresses developed, particularly along the SiC/solder and passivation interfaces.

At the end of a thermal cycle, the maximum observed plastic strain is on the order of 5%, localized on a stress concentration point, at the SiC/solder interface.

Consequently, residual stress distributions at the end of the cooling phase were minimal but not negligible. This confirms that a single thermal cycle, under the assumed conditions, induces limited irreversible mechanical damage, although repeated cycles would likely lead to fatigue accumulation over time.

From the presented results, it can be inferred that the solder remains the layer most prone to the accumulation of plastic strain, leading possible ductile damage phenomena and thermal fatigue, while the die and its passivation layers might be prone to delamination due to the high normal and shear stress gradients across its thickness.

In summary, the results underline the critical role of temperature gradients, not only in magnitude but also in their temporal evolution and in generating stress and plastic strain distributions within power electronic packages. The developed modeling approach allows us to capture the primary effects of non-uniform and transient thermal fields, laying the groundwork for structural integrity predictions and reliability assessments under specific real power cycling conditions.

**Author Contributions:** Conceptualization, G.M. and R.B.; methodology, G.M., G.B. and R.B.; investigation, G.B. and R.B.; resources, G.M.; writing—original draft preparation, G.B. and R.B.; writing—review and editing, G.M., G.B. and R.B.; visualization, G.B. and R.B.; supervision, G.M.; project administration, G.M.; funding acquisition, G.M.; All authors have read and agreed to the published version of the manuscript.

**Funding:** This work has been partially funded by the European Union (NextGeneration EU), through the MUR-PNRR project SAMOTHRACE (ECS00000022).

**Institutional Review Board Statement:** Not applicable.

**Informed Consent Statement:** Not applicable.

**Data Availability Statement:** The presented data are available on request.

**Conflicts of Interest:** The authors declare no conflicts of interest.

## References

1. Yang, Y.; Dorn-Gomba, L.; Rodriguez, R.; Mak, C.; Emadi, A. Automotive Power Module Packaging: Current Status and Future Trends. *IEEE Access* **2020**, *8*, 160126–160144. [CrossRef]
2. Chen, C.; Luo, F.; Kang, Y. A Review of SiC Power Module Packaging: Layout, Material System and Integration. *CPSS Trans. Power Electron. Appl.* **2017**, *2*, 170–186. [CrossRef]
3. Lee, H.; Smet, V.; Tummala, R. A Review of SiC Power Module Packaging Technologies: Challenges, Advances, and Emerging Issues. *IEEE J. Emerg. Sel. Top. Power Electron.* **2020**, *8*, 239–255. [CrossRef]
4. Matallana, A.; Ibarra, E.; López, I.; Andreu, J.; Garate, J.I.; Jordà, X.; Rebollo, J. Power Module Electronics in HEV/EV Applications: New Trends in Wide-Bandgap Semiconductor Technologies and Design Aspects. *Renew. Sustain. Energy Rev.* **2019**, *113*, 109264. [CrossRef]
5. Mirone, G.; Barbagallo, R.; Bua, G.; Sitta, A.; Calabretta, M.; Sequenzia, G. Thermal-Structural Modeling of Power Electronic Package: Effects of Deposition Geometry and Dry Spot on the Stress Distributions. In *Proceedings of the IOP Conference Series: Materials Science and Engineering*; IOP Publishing: Bristol, UK, 2024; Volume 1306, p. 012012.
6. Mirone, G.; Barbagallo, R.; Corallo, L.; Bua, G.; La Rosa, G.; Fargione, G.; Giudice, F. Nonlinear Elastoplastic Response and Damage Modeling in Power Electronics Packages Under Thermal Cycling. *Eng. Proc.* **2025**, *85*, 50. [CrossRef]
7. Mirone, G.; Barbagallo, R.; Bua, G.; La Rosa, G. Finite Element Simulation and Sensitivity Analysis of the Cohesive Parameters for Delamination Modeling in Power Electronics Packages. *Materials* **2023**, *16*, 4808. [CrossRef] [PubMed]
8. Kundu, A.; Balamurali, A.; Korta, P.; Iyer, K.L.V.; Kar, N.C. An Approach for Estimating the Reliability of IGBT Power Modules in Electrified Vehicle Traction Inverters. *Vehicles* **2020**, *2*, 413–423. [CrossRef]

9. Agirrezabala, E.; Aizpuru, I.; Garrido, D.; Portillo, A. Reliability of Power Semiconductor Modules: A State-of-the-Art Review. *IEEE Open J. Power Electron.* **2025**, *6*, 1036–1067. [CrossRef]
10. Lee, C.-C.; Tsai, W.-C.; Chuang, J.-C. Mechanical Reliability of High-Power Modules via Simulation-Based Machine Learning. *Eng. Appl. Artif. Intell.* **2025**, *154*, 111019. [CrossRef]
11. Durand, C.; Klingler, M.; Coutellier, D.; Naceur, H. Power Cycling Reliability of Power Module: A Survey. *IEEE Trans. Device Mater. Reliab.* **2016**, *16*, 80–97. [CrossRef]
12. Otto, A.; Rzepka, S.; Wunderle, B. Investigation of Active Power Cycling Combined With Passive Thermal Cycles on Discrete Power Electronic Devices. *J. Electron. Packag.* **2019**, *141*, 031012. [CrossRef]
13. ECPE Guideline AQG 324 Qualification of Power Modules for Use in Power Electronics Converter Units in Motor Vehicles. Available online: https://www.ecpe.org/index.php?eID=dumpFile&t=f&f=46275&token=0d6454cead46e7321e58907672861b3fcd13c0c0 (accessed on 19 January 2025).
14. Kabaar, A.B.; Buttay, C.; Dezellus, O.; Estevez, R.; Gravouil, A.; Gremillard, L. Characterization of Materials and Their Interfaces in a Direct Bonded Copper Substrate for Power Electronics Applications. *Microelectron. Reliab.* **2017**, *79*, 288–296. [CrossRef]
15. MatWeb: Overview of the Properties of Eutectic Solder (63Sn-37Pb)—ASTM B 32 Grade Sn63. Available online: https://www.matweb.com/search/datasheet.aspx?matguid=3a5c8bc670914d588b26ab0b994d88cb (accessed on 19 January 2025).
16. Agag, T.; Koga, T.; Takeichi, T. Studies on Thermal and Mechanical Properties of Polyimide–Clay Nanocomposites. *Polymer* **2001**, *42*, 3399–3408. [CrossRef]
17. He, J.; Ling, Y.; Lei, D. Mechanical Properties of Sn–Pb Based Solder Joints and Fatigue Life Prediction of PBGA Package Structure. *Ceram. Int.* **2023**, *49*, 27445–27456. [CrossRef]
18. Munro, R.G. Material Properties of a Sintered α-SiC. *J. Phys. Chem. Ref. Data* **1997**, *26*, 1195–1203. [CrossRef]
19. Ucar, Y.; Akova, T.; Aysan, I. Mechanical Properties of Polyamide Versus Different PMMA Denture Base Materials. *J. Prosthodont.* **2012**, *21*, 173–176. [CrossRef] [PubMed]
20. Tsiafis, I.; Bouzakis, K.-D.; Michailidis, N. Determination of Epoxy Resins' Mechanical Properties by Experimental-Computational Procedures in Tension. *J. Balk. Tribol. Assoc.* **2009**, *15*, 18–24.
21. MatWeb: Overview of Materials for Epoxy Molding Compound. Available online: https://www.matweb.com/search/datasheet.aspx?matguid=d32b84b0ef1e410596e9dda9e02429c7 (accessed on 19 January 2025).
22. Matsui, M.; Masuda, M. Fracture Behavior of Silicon Nitride at Elevated Temperatures. In *Tailoring of Mechanical Properties of $Si_3N_4$ Ceramics*; Hoffmann, M.J., Petzow, G., Eds.; Springer Netherlands: Dordrecht, The Netherlands, 1994; pp. 403–414.


**Disclaimer/Publisher's Note:** The statements, opinions and data contained in all publications are solely those of the individual author(s) and contributor(s) and not of MDPI and/or the editor(s). MDPI and/or the editor(s) disclaim responsibility for any injury to people or property resulting from any ideas, methods, instructions or products referred to in the content.